Electronic Supplementary Material (ESI) for Materials Advances.


Supporting Information

# Capacity and Phase Stability of Metal-Substituted α-$Ni(OH)_2$ Nanosheets in Aqueous Ni–Zn Batteries

Samuel W. Kimmel,[a,b] Brandon J. Hopkins,[b,c] Christopher N. Chervin,[b] Nathaniel L. Skeele,[b]

Jesse S. Ko,[b,d] Ryan H. DeBlock,[b] Jeffrey W. Long,[b] Joseph F. Parker,[b] Bethany M. Hudak,[e]

Rhonda M. Stroud,[e] Debra R. Rolison,[b]* and Christopher P. Rhodes[a]*

[a] Department of Chemistry and Biochemistry and Materials Science, Engineering, and Commercialization Program, Texas State University, San Marcos, TX, 78666, USA

[b] U.S. Naval Research Laboratory, Surface Chemistry Branch (Code 6170), Washington, D.C. 20375, USA

[c] NRL-National Research Council Postdoctoral Associate

[d] Former NRL-National Research Council Postdoctoral Associate

[e] U.S. Naval Research Laboratory, Materials Science and Technology Division (Code 6300), Washington, D.C. 20375, USA

*corresponding authors: cprhodes@txstate.edu; debra.rolison@nrl.navy.mil

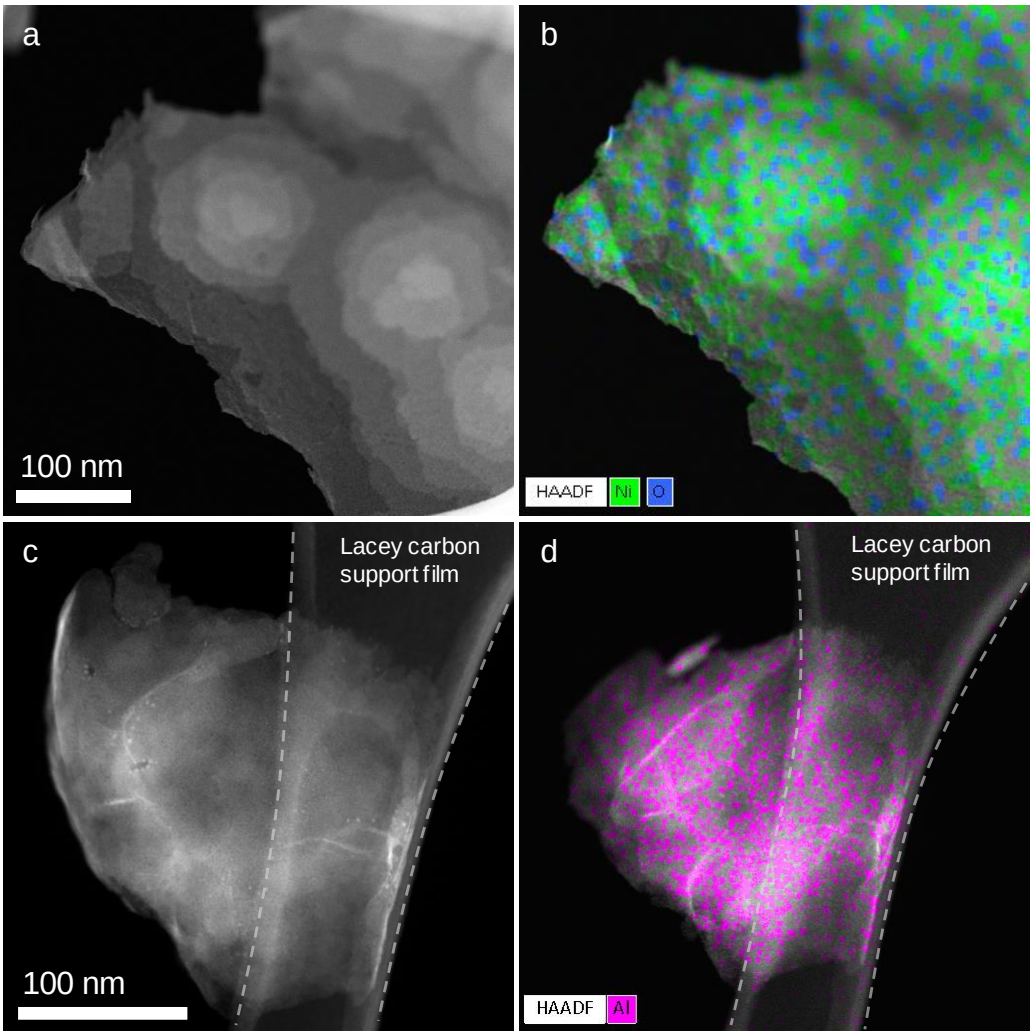


**Fig. S1** High-angle annular dark field (HAADF) and scanning transmission electron microscopy–energy-dispersive spectroscopy (STEM-EDS) images, respectively, of nanosheets of (a, b) α-$Ni(OH)_2$ and (c, d) $Al^{3+}$-substituted α-$Ni(OH)_2$. All samples contain uniform Ni and O distribution and a layered structure; (d) indicates uniform Al distribution. Lacey carbon support film outlined in dashed lines in (c, d).

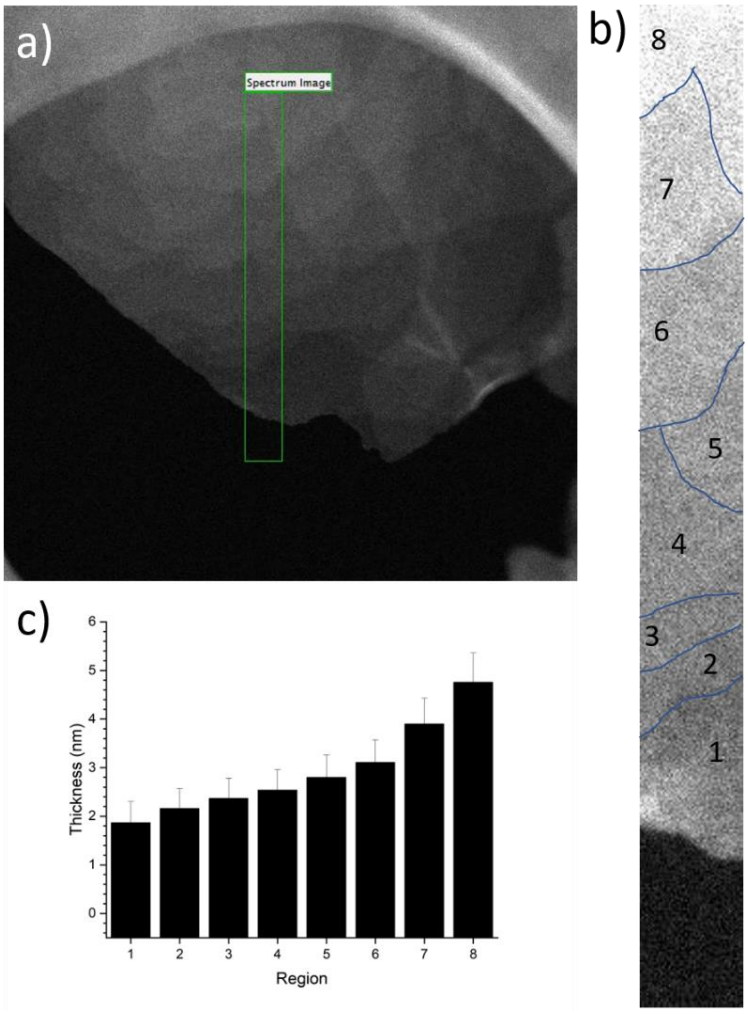


**Fig. S2** $\alpha$-$Ni(OH)_2$ sheet thickness analysis: (a) HAADF image showing layers and region (green box inset) from which an electron energy–loss spectrum was acquired; (b) EELS absolute thickness map calculated from EELS spectrum; (c) bar graph of thickness mean and standard deviation taken from the regions (1–8) demarcated in the EELS thickness map in (b).

**Table S1** Mean thickness and standard deviation of layers in Fig. S2. Layer thickness is calculated by taking the difference between subsequent layers.

| Region | Total Layer Thickness (nm) | Standard Deviation (nm) | Layer thickness (nm) | Number of layers |
|---|---|---|---|---|
| 1 | 1.87 | 0.43 | – | 6 |
| 2 | 2.16 | 0.41 | 0.29 | 7 |
| 3 | 2.37 | 0.41 | 0.21 | 8 |
| 4 | 2.54 | 0.42 | 0.17 | 9 |
| 5 | 2.80 | 0.46 | 0.26 | 10 |
| 6 | 3.11 | 0.46 | 0.31 | 11 |
| 7 | 3.90 | 0.53 | 0.79 | 13 |
| 8 | 4.76 | 0.60 | 0.86 | 15 |

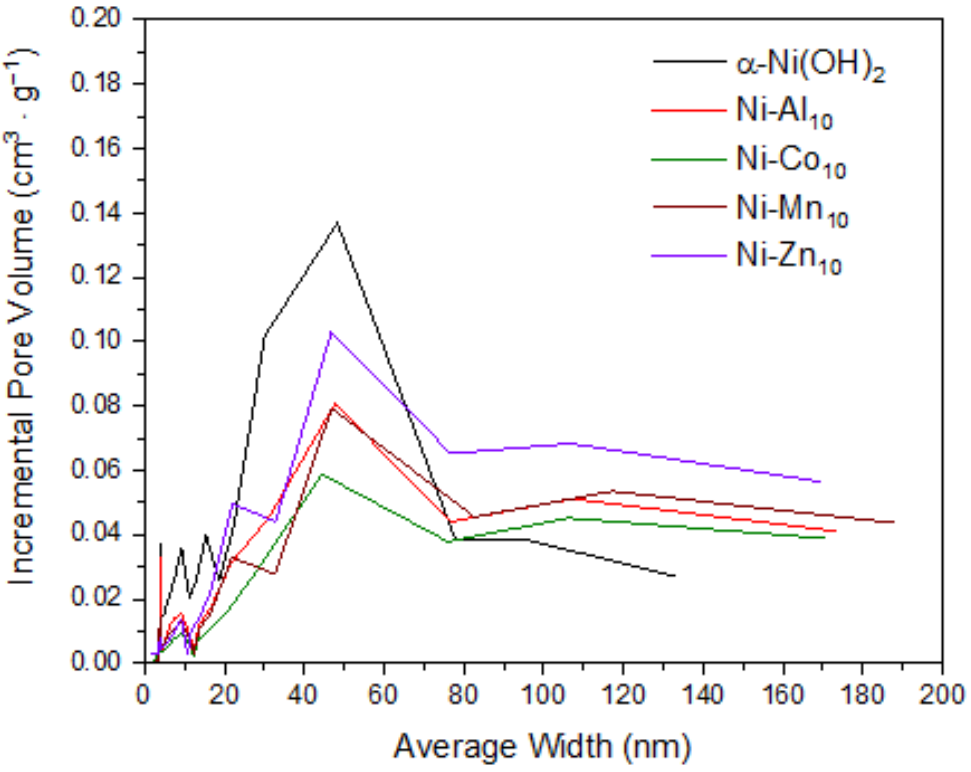


**Fig. S3** Comparison of plots of incremental pore volume versus average pore width determined using Barrett–Joyner–Halenda analysis of the desorption branch of isotherms obtained for nanosheets of α-Ni(OH)$_2$, aluminum-substituted (Ni-Al$_{10}$), cobalt-substituted (Ni-Co$_{10}$), manganese-substituted (Ni-Mn$_{10}$), and zinc-substituted (Ni-Zn$_{10}$)**.**

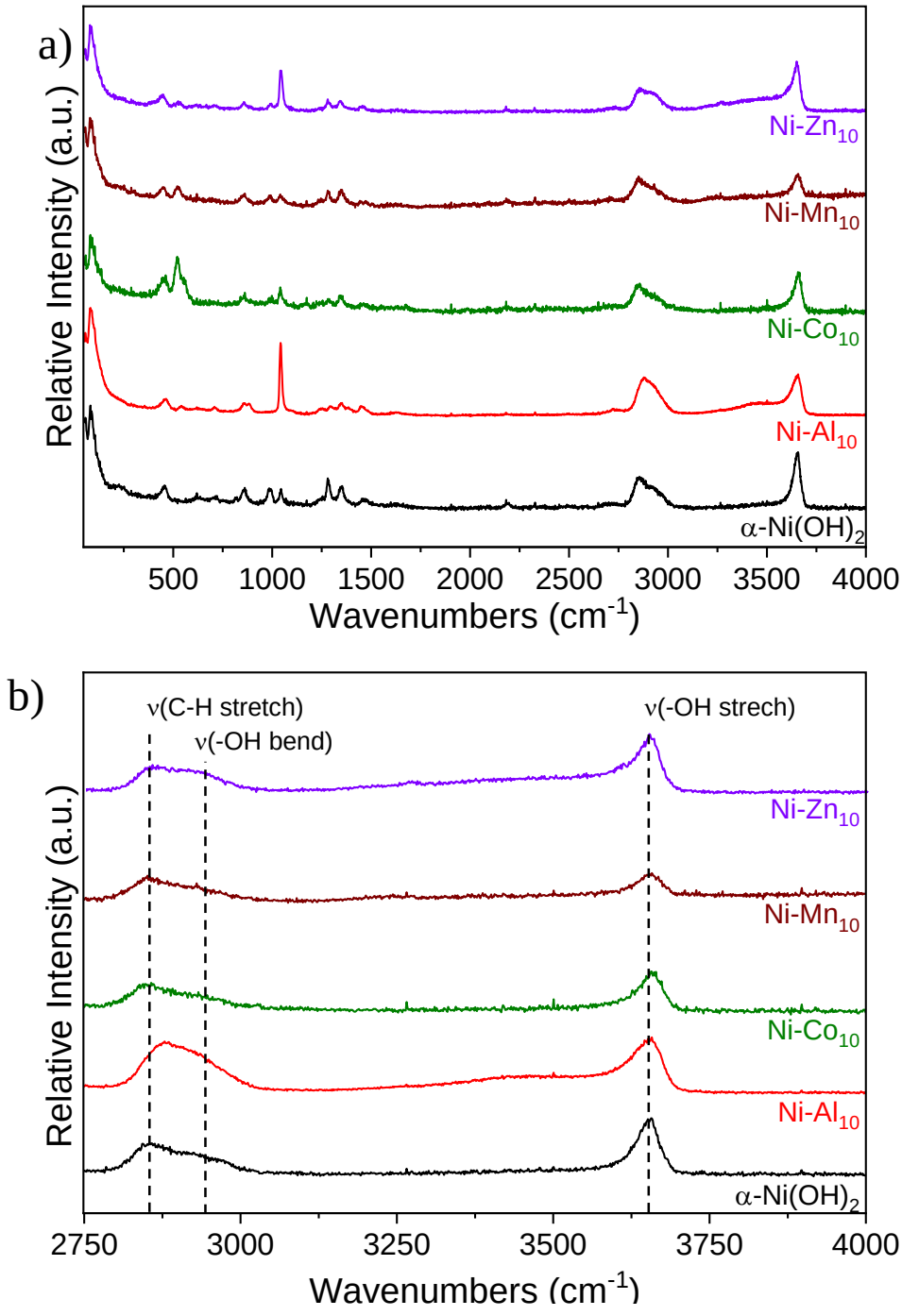


**Fig. S4** Raman spectra of nanosheets of α-$Ni(OH)_2$, aluminum-substituted ($Ni\text{-}Al_{10}$), cobalt-substituted ($Ni\text{-}Co_{10}$), manganese-substituted ($Ni\text{-}Mn_{10}$), and zinc-substituted ($Ni\text{-}Zn_{10}$): (a) full spectrum from 50 $cm^{-1}$ to 4000 $cm^{-1}$; and (b) expanded spectral region between 2750 $cm^{-1}$ to 4000 $cm^{-1}$.

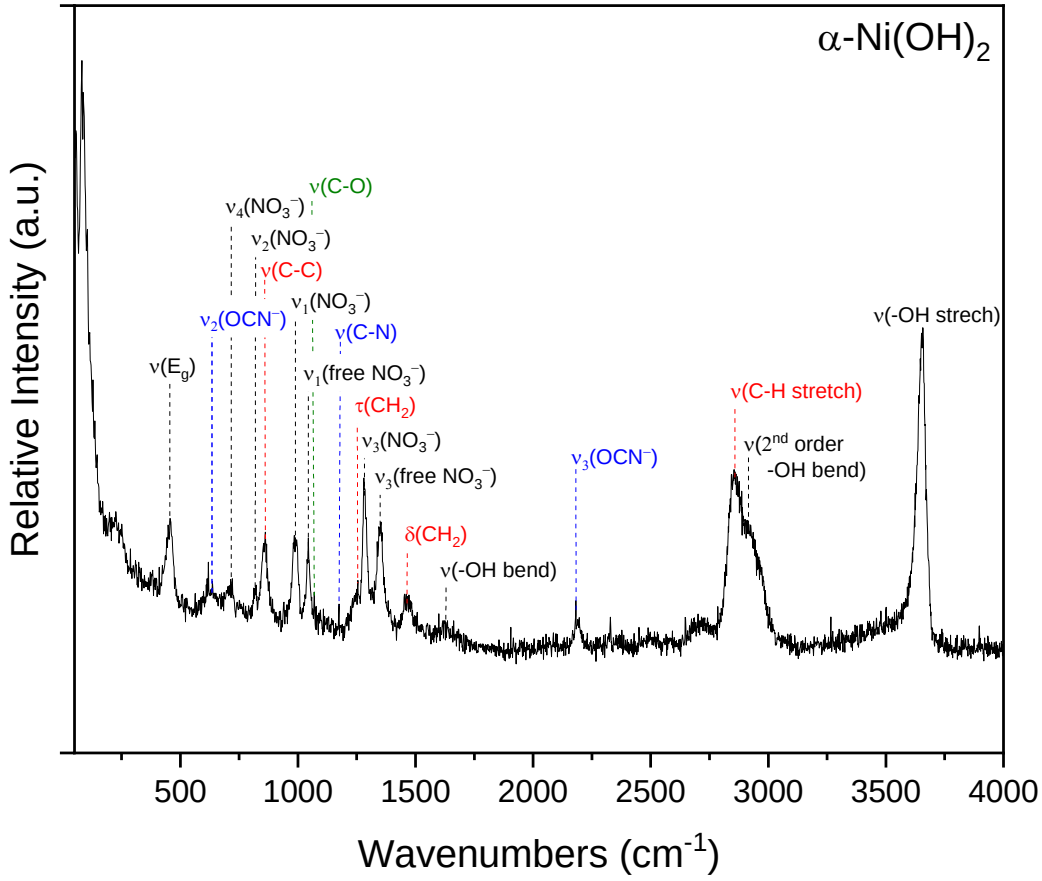


**Fig. S5** Raman spectrum of unsubstituted α-$Ni(OH)_2$ nanosheets from 50 $cm^{-1}$ to 4000 $cm^{-1}$; spectrum obtained using a laser excitation frequency of 514 nm.

**Table S2** Raman peaks for microwave-synthesized unsubstituted α-$Ni(OH)_2$ nanosheets within the 50 $cm^{-1}$ to 4000 $cm^{-1}$ region, peak assignments, experimental wavenumbers and reported wavenumbers from the literature.

| Signal Source | Peak Assignment | Experimental wavenumber ($cm^{-1}$) | Reported wavenumber ($cm^{-1}$) |
|---|---|---|---|
| α-$Ni(OH)_2$ lattice | $\nu(E_g)$ | 458 | 460 [1]<br>474 [2] |
| | $\nu(A_{1g})$ | – | 495 [1]<br>554 [2] |
| | ν(–OH bend) | 1625 | 1620 [1] |
| | $\nu(2^{nd}$ order –OH bend) | 2914 | ~ 2900 [1] |
| | ν(–OH stretch) | 3657 | 3647 [1] |
| Nickel-nitrate precursor | $\nu_1(NO_3^-)$ | 986 | 997 [1] |
| | $\nu_2(NO_3^-)$ | 821 | 816 [1] |
| | $\nu_3(NO_3^-)$ | 1283 | 1291 [1] |
| | $\nu_4(NO_3^-)$ | 721 | 719 [1] |
| | $\nu_1$(free $NO_3^-$) | 1042 | 1047 [1] |
| | $\nu_3$(free $NO_3^-$) | 1352 | 1350 [1] |
| Ethylene glycol precursor | ν(C–C) | 861 | 864 [3] |
| | $\tau(C–H_2)$ | 1254 | 1260 [3] |
| | $\delta(C–H_2)$ | 1464 | 1459 [3] |
| | ν(C–H) | 2854 | 2875 [3] |
| Urea precursor | ν(C–N) | 1173 | 1177 [4] |
| | $\nu_2(OCN^-)$ | 636 | 630–632 [5] |
| | $\nu_3(OCN^-)$ | 2181 | 2160–2180 [5,6] |
| Carbonate | ν(C–O) | 1069 | 1066 [7,8] |

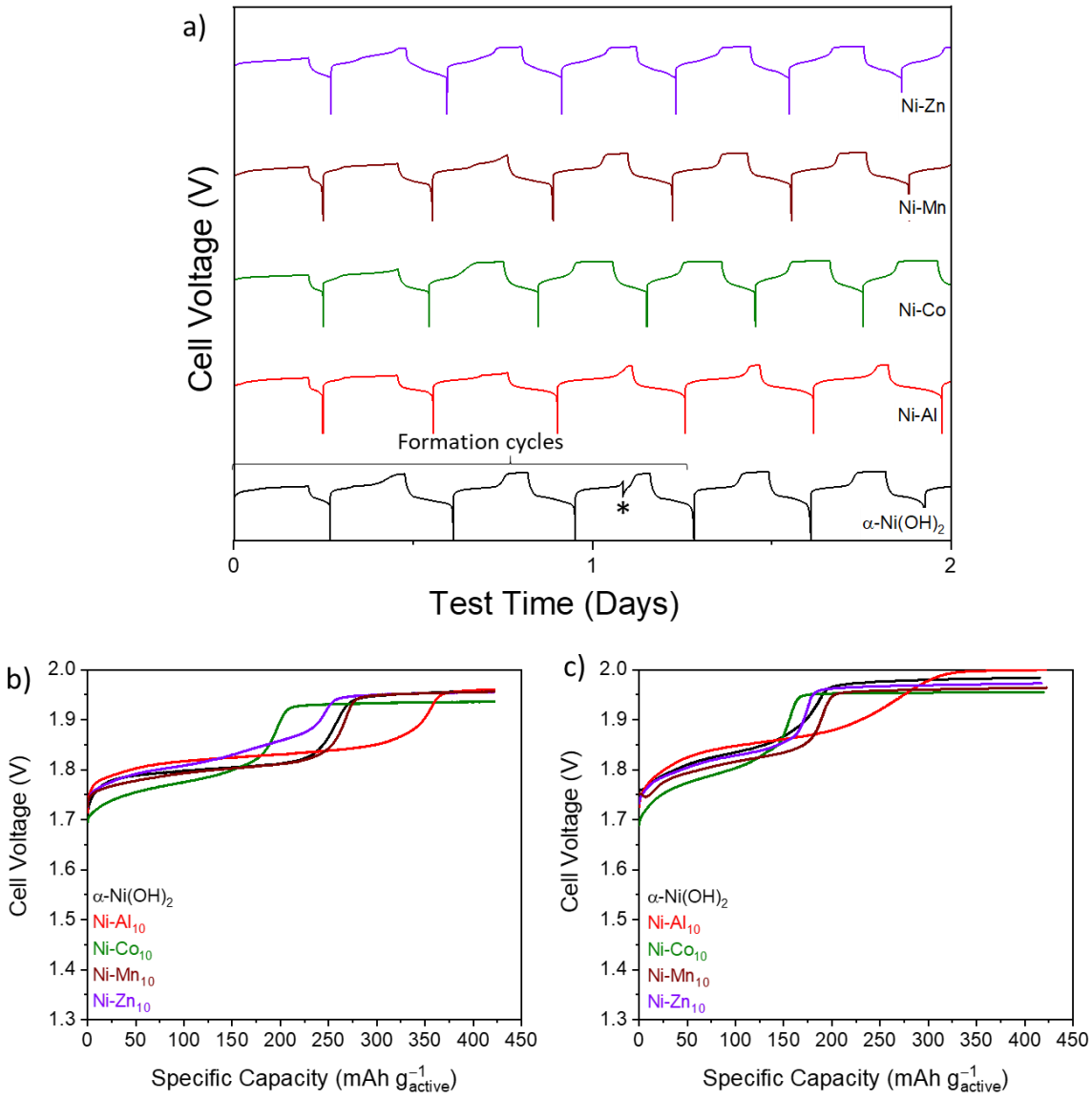


**Fig. S6** (a) Plots of cell voltage versus test time showing formation cycling of Ni–Zn sponge cells at a mass-normalized current of 84.4 mA $g^{-1}_{active}$ between 1.3–2.0 V vs Zn; the cells are equipped with powder-composite cathodes containing nanosheets of unsubstituted α-$Ni(OH)_2$, aluminum-substituted ($Ni\text{-}Al_{10}$), cobalt-substituted ($Ni\text{-}Co_{10}$), manganese-substituted ($Ni\text{-}Mn_{10}$), or zinc-substituted ($Ni\text{-}Zn_{10}$). The cells are charged up to 2.0 V or until reaching a theoretical capacity of 422 mAh $g^{-1}_{active}$; * indicates a short power outage; comparison of the cell voltage versus specific capacity plots for the 5$^{th}$ cycle (b) and 35$^{th}$ cycle (c) charging steps.

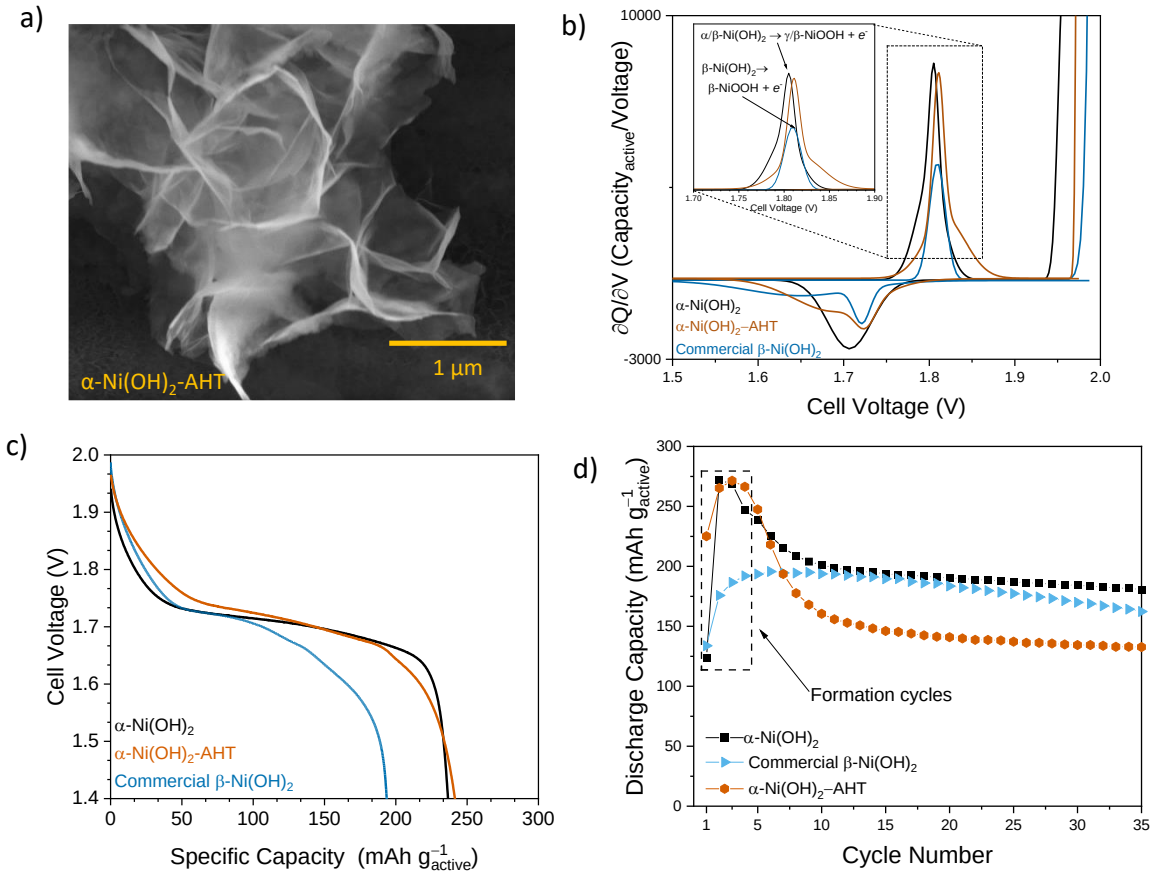


**Fig. S7** (a) Scanning electron micrograph of hydrothermally treated α-$Ni(OH)_2$ nanosheets (α-$Ni(OH)_2$-AHT); (b) comparison of 5$^{th}$ cycle differential capacity ($\partial Q/\partial V$) plots of α-$Ni(OH)_2$ nanosheets, α-$Ni(OH)_2$-AHT nanosheets, and commercial β-$Ni(OH)_2$ (Alfa); (c) comparison of 5$^{th}$ cycle voltage vs. specific capacity of α-$Ni(OH)_2$ nanosheets, α-$Ni(OH)_2$-AHT nanosheets, and commercial β-$Ni(OH)_2$ (Alfa); and (d) comparison of specific discharge capacity vs. cycle number of α-$Ni(OH)_2$ nanosheets, α-$Ni(OH)_2$-AHT nanosheets, and commercial β-$Ni(OH)_2$ (Alfa); cells were charged and discharged at a mass-normalized current rate of 84.4 mA $g^{-1}_{active}$ between 1.3 and 2.0 V.

## References


1. D. S. Hall, D. J. Lockwood, S. Poirier, C. Bock and B. R. MacDougall, Raman and Infrared Spectroscopy of Alpha and Beta Phases of Thin Nickel Hydroxide Films Electrochemically Formed on Nickel, *J. Phys. Chem. A*, 2012, **116**, 6771-6784.
2. D. Chen, X. Xiong, B. Zhao, M. A. Mahmoud, M. A. El-Sayed and M. Liu, Probing Structural Evolution and Charge Storage Mechanism of $NiO_2H_x$ Electrode Materials using In Operando Resonance Raman Spectroscopy, *Adv. Sci.*, 2016, **3**, 1500433-1500436.
3. W. Sawodny, K. Niedenzu and J. W. Dawson, The Vibrational Spectrum of Ethylene Glycol, *Spectrochim. Acta A Mol. Biomol. Spectrosc.*, 1967, **23**, 799-806.
4. B. Rousseau, R. Keuleers, H. O. Desseyn, H. J. Geise and C. Van Alsenoy, Solids Modeled by Ab-Initio Crystal Field Methods. Effects of Intermolecular Interactions on the Vibrational Spectrum of Urea, *Chem. Phys. Lett.*, 1999, **302**, 55-59.
5. M. H. Brooker and N. Wen, Raman Studies of Cyanate: Fermi Resonance, Hydration and Hydrolysis to Urea, *Can. J. Chem.*, 1993, **71**, 1764-1773.
6. F. F. Cleveland, Raman Spectrum of an Aqueous Solution of Potassium Cyanate, *J. Am. Chem. Soc.*, 1941, **63**, 622-623.
7. Y. Ma, W. Yan, Q. Sun and X. Liu, Raman and Infrared Spectroscopic Quantification of the Carbonate Concentration in $K_2CO_3$ Aqueous Solutions with Water as an Internal Standard, *Geosci. Front.*, 2021, **12**, 1018-1030.
8. J. Wu and H. Zheng, Quantitative Measurement of the Concentration of Sodium Carbonate in the System of $Na_2CO_3$–$H_2O$ by Raman spectroscopy, *Chem. Geol.*, 2010, **273**, 267-271.